ORIGINAL PAPER

Omar S. Hussein ⬤

Aeroelastic analysis of membrane airfoils and flexible-chord airfoils with trailing-edge flaps

Abstract This paper studies the static and dynamic aeroelastic characteristics of membrane airfoils and flexible-chord airfoils (deformable airfoils) with the emphasis on the effects of a trailing-edge (TE) flap which is a novel topic. Two modeling approaches are presented; the first method is the Rayleigh–Ritz method, and the second method is the finite element method which is an efficient method to study the TE flap effects. The two models are presented in the Laplace domain which enables the transient response analysis. The models adopt the potential flow aerodynamics based on the Prandtl–Glauert thin-airfoil theory and the Theodorsen's unsteady theory. The airfoils are assumed to have small deformations, so linear structural models are used. The effect of the airfoils' flexibilities on the static aeroelastic characteristics and the dynamic responses due to step and harmonic TE flap inputs is presented through a parametric study.

1 Introduction

The interest in the design of micro-air vehicles (MAVs) and the increasing flexibility of modern aircraft has led aerospace engineers and scientists to study the aerodynamic characteristics of flexible airfoils overs several decades. There are two types of flexible airfoils; the first one is the membrane airfoil which is a type of two-dimensional structures with a very thin thickness such that its bending stiffness is negligible, so it supports the applied external transverse loads by the in-plane tension forces throughout the curvature of its deformed shape. In the field of aerospace engineering, parachutes, hang gliders, and some micro-air vehicles are examples of membrane structures and in nature, wings of insects and bats are perfect examples of membrane wings. The second type is the flexible-chord airfoil which is an airfoil with low bending stiffness such that it suffers from camber deformations due to the air flow. Such airfoils are used also for the design of MAVs with very thin plate-like wings or for larger morphing air vehicles where the airfoil internal structure flexibility is designed to be low to allow passive or active morphing capabilities [1].

The aeroelastic analysis of membranes has been an ongoing research since the beginning of the nineteenth century by studying parachutes and yacht sails performances [2–5]. Nowadays, the development of micro-air vehicles and the desire to imitate the performance of flying insects, birds, or animals has attracted the interests of many researchers in the past few years [6]. One of the earliest work in the field membrane airfoil aeroelasticity is the work of Thwaites [7] where an analytical solution was presented to get a relation between the static membrane deformation and the applied aerodynamic loading. The linear sail differential equation was used along with the potential flow theory. The work of Nielsen [8] also theoretically studied the linear static aeroelastic behavior of membrane airfoils and compared the results with experiments. The Fourier series expansion was used to solve the sail governing differential equation and the thin-airfoil theory was adopted to model the aerodynamic loading. The theoretical static deformation shape of the airfoil and the lift coefficient

O. S. Hussein (✉)
Lecturer at the Aerospace Engineering Department, Cairo University, Giza, Egypt
e-mail: aero.omarshukry@cu.edu.eg; aero.omarshukry@gmail.com

were in a good agreement with the experiments for the range of Reynold's number 5.6–7.8 $(10)^5$ and for maximum camber less than 15%. Jackson [9] assumed the deformed membrane to be a cubic function with two unknown coefficients. These coefficients were estimated by a method of aerodynamic forces balancing and geometric constraints. Newman and Low [10] used potential thin-airfoil theory as Nielson and Thwaites did, but they applied the Kutta condition at the leading edge instead of the trailing edge in an effort to simulate the effect of the boundary layer bubble at the trailing edge. The theoretical results were compared with experiments for four excess-length ratios, but not good agreement was found. Unlike the previously mentioned models where the potential thin-airfoil theory with continuous vortex sheet along the airfoil chord was used for the aerodynamic modeling, Greenhalgh et al. [11] used a discrete vortex sheet by dividing the membrane chord into number of segments with a concentrated vortex located at the quarter point of each segment. A good match with the experimental results was reported for small angle of attacks.

Newman and Paidousses [12] studied the dynamic instability (Luffing) of membrane sail under very low tension forces. An approximate analytical closed form solution using the potential flow theory was presented to specify the stability limits. Mavroyiakoumou and Alben [13, 14] studied the stability of membrane airfoils with different types of boundary conditions: fixed–fixed, fixed–free, and free–free edges. Inviscid potential flow model including the wake effect of Saffman [15] was used. Starting by the membrane differential equation, a nonlinear eigen-value problem was derived that was solved iteratively to estimate the stability limits. Sygulski [16] presented an integral aeroelastic formulation that was solved by the boundary element method and a differential equation formulation that was solved by the finite difference method. Potential flow theory with wake modeling was used. Tiomkin and Raveh [17] presented a Laplace domain formulation based on the Fourier series solution adopted by Nielsen [8] and the Schwarz's unsteady aerodynamic model. The static and dynamic stability limits of membrane airfoils were studied for different values of the membrane mass density. Tsesana and Breuer [18] studied the steady and unsteady aeroelastic behaviors of flapping membrane airfoils at different frequencies. The membrane deformation was represented by a series solution, and the potential flow model of Wu [19] was chosen to estimate the unsteady aerodynamic loadings. The resulting aeroelastic ordinary differential equation was solved by the Chebyshev collocation method iteratively. Recently, Hussein [20] proposed a finite element formulation to study the aeroelasticity of membrane airfoils with elastic boundary conditions using the potential flow aerodynamics which is extended in this work to model membrane and deformable airfoils with TE flaps.

Another approach for the aerodynamic modeling of membrane airfoils is based on computational fluid dynamics models (CFD) to capture some effects that cannot be predicted by the inviscid potential flow method like the effect of the leading- and trailing-edge shape [21], the viscous effects [22–24], and large angle of attacks [25].

Moving to the analysis of deformable airfoils, Su [26] developed an aeroelastic model of flexible-chord airfoils using Legendre polynomial series representation of the airfoil camber deformation and the finite-states potential flow theory of Johnson and Peters [27] to capture the unsteady aerodynamic loadings on the airfoil. The Hamilton's principle was used to derive the system of differential equations describing the aeroelastic problem. Walker and Patil [28] studied the unsteady aerodynamics of deformable thin airfoils where the camber deformation is presumed and represented by Chebyshev polynomials series. An aerodynamic theory is derived to estimate the lift, moment, and thrust generated by a harmonically deformed airfoil. Murua et al. [29] analyzed the effect of the camber deformation on the dynamic instability (flutter) of airfoils. The airfoil camber deformation is predefined by a single symmetric quadratic function besides the two rigid-body degrees of freedom and the airfoil was supported by two translational springs at equal distances from the mid-chord point. Berci et al. [30] proposed a semi-analytical method to study the aeroelastic instability and response of flexible airfoils. The finite-states inflow theory of Peters was used to estimate the unsteady aerodynamic loading. The camber deformation is represented by Chebyshev polynomials, and the aeroelastic system of equation is derived using the Ritz method. Riso et al. [31] also presented a semi-analytical formulation for the unsteady aerodynamics of flexible flat plate airfoils. A potential flow conformal mapping technique is derived to estimate the aerodynamic coefficients for a cantilevered flexible airfoil with a predefined deformation. CFD approaches are also available in the literature to study the aerodynamics of deformable airfoils [32–34].

The present work studies the static and dynamic aeroelastic responses of membrane and flexible-chord airfoils with TE flaps which have not been covered before in literature. The aeroelastic formulation is derived and presented using the Rayleigh–Ritz approach and the finite element approach. The Theodorsen's unsteady aerodynamic theory and the Prandtl–Glauert thin-airfoil theory are used to present the aerodynamic loading in an efficient matrix form in terms of the airfoil degrees of freedom. The static, transient, and frequency

responses of the flexible airfoils due to step and harmonic TE flap inputs are presented and discussed via a parametric analysis.

2 Rayleigh–Ritz formulation

2.1 Flapless airfoils

The aeroelastic modeling of flexible airfoils without a trailing-edge flap can be done using the Rayleigh–Ritz approach which approximates the global deformation as a series solution with coefficients to be determined using the Euler–Lagrange equation which can be in terms of the elastic strain energy (U), the Kinetic energy ($\mathcal{K}$), and the external work done (W) as follows:

$$\frac{\partial U}{\partial \eta_n} + \frac{d}{dt}\left(\frac{\partial \mathcal{K}}{\partial \dot{\eta}_n}\right) = \frac{\partial W}{\partial \eta_n}, \quad n = 1, 2, \dots, n_s \tag{1}$$

where η_n are the coefficients of the series solution expansion which can be written for a membrane airfoil with (n_s) terms shown in Fig. 1 as follows:

$$w(x,t) = \sum_{n=1}^{n_s} \eta_n(t)\varphi_n(x), \quad \varphi_n(x) = \sin\left(\frac{n\pi x}{c}\right) \tag{2}$$

For a membrane airfoil with a chord (c) and mas per unit length (ϱ) that is subjected to a tension force (T) and an aerodynamic pressure $p(x, t)$, the elastic strain energy, the kinetic energy, and the external work can be written as follows:

$$U = \frac{T}{2}\int_0^c w,_x^2 \, dx, \quad \mathcal{K} = \frac{\varrho}{2}\int_0^c \dot{w}^2 \, dx, \quad W = \int_0^c p(x,t)w \, dx \tag{3}$$

Substituting Eqs. (2) and (3) into Eq. (1) yields the governing equations of motion which can be written in the matrix form as follows:

$$[M]\left\{\ddot{\vec{\eta}}_n\right\} + [K]\{\vec{\eta}_n\} = \int_0^c p(x,t)\{\vec{\varphi}_n(x)\} \, dx, \quad n = 1, 2, \dots\dots n_s \tag{4}$$

The mass matrix $[M]$ and the stiffness matrix $[K]$ are given in Appendix. The pressure term in Eq. (4) has three components: the quasi-steady $p^{QS}(x, t)$, the added mass $p^{\mathcal{M}}(x, t)$, and the wake component $p^{\mathcal{W}}(x, t)$. The quasi-steady aerodynamic pressure distribution is modeled using the Prandtl–Glauert thin-airfoil potential flow theory which estimates the pressure due to a sheet of bound vortices $\gamma_b(x, t)$ and a free stream dynamic pressure $\left(q_\infty = \frac{1}{2}\rho_\infty V_\infty^2\right)$ using a finite series solution with n_a+1 terms and a transformed coordinate $\theta = a\cos\left(1 - \frac{2x}{c}\right)$ as follows [35]:

$$p^{QS}(x,t) = 4q_\infty \left\lfloor \frac{1+\cos(\theta)}{\sin(\theta)} \; \sin(\theta) \; \sin(2\theta) \; \dots \; \sin(n_a\theta) \right\rceil \left\{\begin{array}{c} A_o \\ A_1 \\ \vdots \\ A_{n_a} \end{array}\right\}, \quad 0 \le \theta \le \pi \tag{5}$$

The aerodynamic series coefficients can be estimated due to the membrane deformation, the airfoil angle of attack (α), and the free stream speed (V_∞) as follows:

$$A_o = \alpha - \frac{1}{\pi}\int_0^\pi \left(w(x,t),_x + \frac{1}{V_\infty}w(x,t),_t\right) d\theta$$

$$A_m = \frac{2}{\pi}\int_0^\pi \left(w(x,t),_x + \frac{1}{V_\infty}w(x,t),_t\right)\cos(m\theta) \, d\theta \tag{6}$$
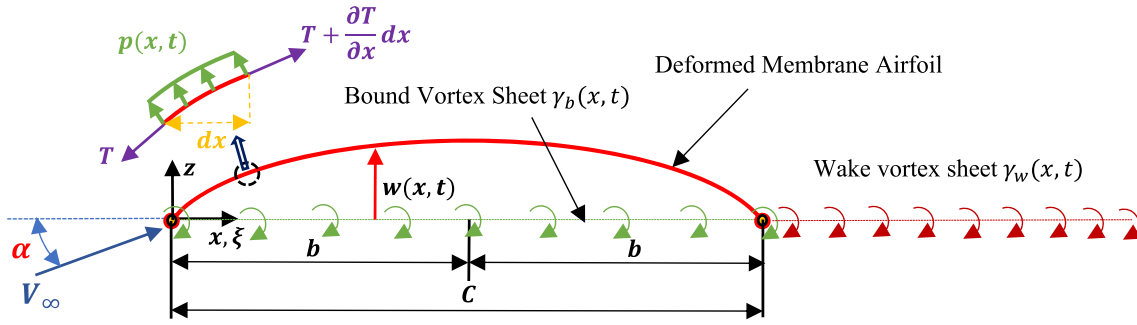
Fig. 1 Membrane airfoil parameters demonstration

Substituting the series representation of the membrane deformation into Eq. (6) gives the following matrix form of the aerodynamic coefficients (see Appendix):

$$\left\{ \begin{array}{c} A_o \\ A_1 \\ \vdots \\ A_{n_a} \end{array} \right\} = \alpha\left\{ \overrightarrow{I_o} \right\} + [\mathcal{A}]\{\vec{\eta}\} + \frac{1}{V_\infty}[\mathcal{B}]\{\dot{\vec{\eta}}\} \tag{7}$$

Substituting Eq. (7) into Eq. (5) yields the following expression for the quasi-steady pressure contribution in Eq. (4):

$$\int_0^c p^{\mathcal{QS}}(x,t)\varphi_n(x)\,\mathrm{d}x = 4q_\infty\lfloor\mathcal{D}_n\rfloor\left(\alpha\left\{\overrightarrow{I_o}\right\} + [\mathcal{A}]\{\vec{\eta}\} + \frac{1}{V_\infty}[\mathcal{B}]\{\dot{\vec{\eta}}\}\right)$$

$$= q_\infty\left(\left\{\vec{f}^{\mathcal{QS}}\right\} + [A_s]\{\vec{\eta}\} + [A_d]\{\dot{\vec{\eta}}\}\right) \tag{8}$$

The Theodorsen's unsteady thin-airfoil theory is used to estimate the added mass aerodynamic pressure coefficient and the wake effect pressure due to a harmonic motion of the membrane surface at a certain reduced frequency $k = \omega b/V_\infty$ which causes a downwash speed amplitude $\overline{w}(x)$ as follows [36, 37]:

$$p^{\mathcal{M}}(x^*,k) = -\frac{4ik}{\pi}\int_{-1}^1 \Lambda(x^*,\xi^*)\frac{\overline{w}(\xi^*)}{V_\infty}\,\mathrm{d}\xi^*$$

$$p^{\mathcal{W}}(x^*,k) = \frac{4}{\pi}[1 - C(k)]\sqrt{\frac{1-x^*}{1+x^*}}\int_{-1}^1 \sqrt{\frac{1+\xi^*}{1-\xi^*}}\frac{\overline{w}(\xi^*)}{V_\infty}\,\mathrm{d}\xi^*,$$

$$x^* = \frac{x}{b} - 1 \tag{9}$$

The Theodorsen's function $C(k)$ and the inertia function $\Lambda(x^*, \xi^*)$ are given in Appendix. The down wash speed amplitude $(\overline{w})$ is related to the membrane surface deformation amplitude $(\overline{w})$ as follows:

$$\overline{w}(x^*) = i\omega\overline{w} + V_\infty\frac{d\overline{w}}{dx} - V_\infty\overline{\alpha}$$

$$= i\omega\sum_{n=1}^{n_s}\overline{\eta}_n(t)\varphi_n(x^*) + V_\infty\sum_{n=1}^{n_s}\overline{\eta}_n(t)\varphi_{n,x}(x^*) - V_\infty\overline{\alpha} \tag{10}$$

Substituting Eq. (9) into Eq. (10) will give the following expressions for the contribution of the added-mass pressure and the wake effect pressure in Eq. (4) as follows:

$$\int_0^c p^{\mathcal{M}}(x^*,t)\{\vec{\varphi}_n(x^*)\}\,\mathrm{d}x = q_\infty\big(k^2[A_{\mathcal{M}1}] + ik[A_{\mathcal{M}2}]\big)\left\{\overrightarrow{\overline{\eta}}\right\} + q_\infty ik\overline{\alpha}\left\{\vec{f}^{\mathcal{M}}\right\} \tag{11}$$

$$\int_0^c p^{\mathcal{W}}(x^*,t)\{\vec{\varphi}_n(x^*)\}\,\mathrm{d}x = q_\infty[1 - C(k)](ik[A_{\mathcal{W}1}] + [A_{\mathcal{W}2}])\left\{\overrightarrow{\overline{\eta}}\right\} + q_\infty[1 - C(k)]\overline{\alpha}\left\{\vec{f}^{\mathcal{W}}\right\} \tag{12}$$
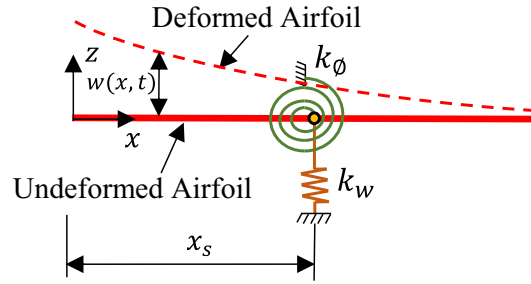
Fig. 2 Flexible-chord airfoil nomenclature

For a flexible-chord airfoil shown in Fig. 2, the deformation can be represented using the free-free vibration mode shapes of an elastic beam as follows [38]:

$$w(x,t) = \sum_{n=-1}^{n_s} \eta_n(t)\varphi_n(x) \tag{13}$$

The functions $\varphi_n(x)$ are as follows:

$$\varphi_{-1}(x) = -(x - x_s), \quad \varphi_0(x) = 1$$

$$\varphi_n(x) = \cos(\lambda_n x) + \cosh(\lambda_n x) - \frac{\cos(\lambda_n c) - \cosh(\lambda_n c)}{\sin(\lambda_n c) - \sinh(\lambda_n c)}$$

$$\times [\sin(\lambda_n x) + \sinh(\lambda_n x)], \quad n = 1, \ldots, n_s \tag{14}$$

where x_s is the location of the point to which the translational and rotational springs are attached which is analogous to the elastic axis of a wing. The parameter λ_n is obtained by solving the following solution:

$$\cos(\lambda_n c)\cosh(\lambda_n c) - 1 = 0 \tag{15}$$

The elastic strain energy of the airfoil is written in terms of the bending stiffness (EI), the translational and rotational springs stiffnesses (k_w, k_ϕ) as follows:

$$U = \frac{EI}{2} \int_0^c w_{,xx}^2 \mathrm{d}x + \frac{1}{2}k_w w^2(x_s) + \frac{1}{2}k_\phi w^2(x_s)_{,x} \tag{16}$$

The expressions of the kinetic energy and the work done are the same as in Eq. (3), so following the exact procedure as in the case of a membrane airfoil, the aeroelastic equations of motion can be easily obtained.

2.2 Flapped airfoils

In order to add the effect of the TE flap shown in Fig. 3, an additional TE deflection function $\varphi_{\mathrm{TE}}(x)$ is introduced which can be written as follows:

$$\varphi_{\mathrm{TE}}(x) = \begin{cases} 0 & x < (1-e)c \\ x - (1-e)c & x \geq (1-e)c \end{cases} \tag{17}$$

So, the generalized force vectors $\{\vec{f}_\beta\}$, $\{\vec{f}_\beta^\mathcal{M}\}$, and $\{\vec{f}_\beta^\mathcal{W}\}$ due to a unit flap deflection can be obtained by substituting $\varphi_n(x)$ in Eqs. (A.2) and (A.3) by $\varphi_{\mathrm{TE}}(x)$ and $\varphi_l(\xi)$ in Eqs. (A.7), (A.8), (A.10) and (A.11) by $\varphi_{\mathrm{TE}}(x)$ which yield the following expressions:

$$\{\vec{f}_\beta\} = 4[\mathcal{D}]\left([\mathcal{A}^{\mathrm{TE}}] + \frac{\mathcal{S}}{V_\infty}[\mathcal{B}^{\mathrm{TE}}]\right)$$

$$\{\vec{f}_\beta^\mathcal{M}\} = -\left(\mathcal{S}\frac{b}{V_\infty}\right)^2 \{f_\beta^{\mathcal{M}1}\} + \mathcal{S}\frac{b}{V_\infty}\{f_\beta^{\mathcal{M}2}\}$$
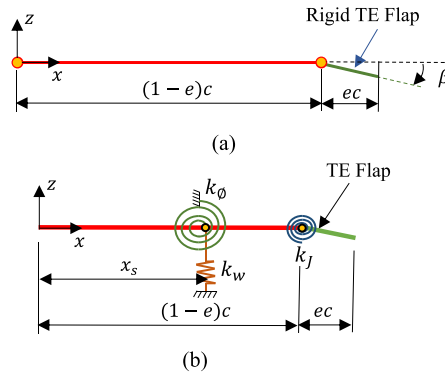
Fig. 3 Airfoils with TE flaps. **a** Membrane airfoil. **b** Flexible-chord airfoil

$$\left\{\vec{f}_\beta^{\mathcal{W}}\right\} = [1 - \mathcal{F}(\mathcal{S})]\left(\mathcal{S}\frac{b}{V_\infty}\left\{f_\beta^{\mathcal{W}1}\right\} + \left\{f_\beta^{\mathcal{W}2}\right\}\right) \tag{18}$$

For the flexible-chord airfoil, the assumed deflection function will be the same as defined in Eq. (14), while for the membrane airfoil, the functions have to be redefined to be as follows:

$$\varphi_n(x) = \begin{cases} \sin\left(\frac{n\pi x}{(1-e)c}\right) & x < (1-e)c \\ 0 & x \geq (1-e)c \end{cases} \tag{19}$$

Therefore, the final governing system of equations of a flapped airfoil can be written in the Laplace-domain matrix form through replacing $i\omega$ by the Laplace variable $(\mathcal{S})$ and using the Laplace form of the Theodorsen's function $\mathcal{F}(\mathcal{S})$ which yields the following form:

$$\mathcal{S}^2\left([M] + \frac{1}{2}\rho_\infty b^2[A_{\mathcal{M}1}]\right)\{\vec{\eta}\}_\mathcal{S} - \mathcal{S}\frac{q_\infty}{V_\infty}([A_d] + b[A_{\mathcal{M}2}] + b[1 - F(\mathcal{S})][A_{\mathcal{W}1}])\{\vec{\eta}\}_\mathcal{S}$$
$$+ ([K] - q_\infty[A_s] - q_\infty[1 - \mathcal{F}(\mathcal{S})][A_{\mathcal{W}2}])\{\vec{\eta}\}_\mathcal{S}$$
$$= q_\infty\left(\frac{\mathcal{S}b}{V_\infty}\left\{\vec{f}^{\mathcal{M}}\right\} + \left\{\vec{f}\right\} + [1 - \mathcal{F}(\mathcal{S})]\left\{\vec{f}^{\mathcal{W}}\right\}\right)\alpha + q_\infty\left(\left\{\vec{f}_\beta\right\} + \left\{\vec{f}_\beta^{\mathcal{M}}\right\} + \left\{\vec{f}_\beta^{\mathcal{W}}\right\}\right)\beta \tag{20}$$

3 Finite element formulation

This section presents the finite element aeroelastic formulation for a membrane airfoil and a flexible-chord airfoil. The airfoil is discretized into (n_s) elements with length (l_e) as shown in Fig. 4. Starting with the modeling of a membrane airfoil, the vertical displacement is approximated over each element in terms of its nodal displacement vector $\left\{\vec{q}_w\right\}_e = \left\{w_{1e}\ w_{2e}\right\}^T$ through a shape function $[N_s]$ as follows [20]:

$$w = \lfloor 1-s\ s \rfloor \begin{Bmatrix} w_{e1} \\ w_{e2} \end{Bmatrix} = [N_s]\{\vec{q}_w\}_e \tag{21}$$

The principle of virtual work is used in this work to derive the elemental matrices. So, the virtual strain energy in a membrane element can be written in terms of the element stiffness matrix $[K_e]$ and the element displacement vector $\left\{\vec{q}_w\right\}_e$ as follows:

$$\delta U^e = \{\delta\vec{q}_w\}_e^T\left(\frac{T}{l_e}\int_0^1 \frac{d[N_s]^T}{ds}\frac{d[N_s]}{ds}\,ds\right)\{q_w\}_e = \{\delta\vec{q}_w\}_e^T[K]_e\{\vec{q}_w\}_e \tag{22}$$

Similarly, the virtual work due the inertial loading (δW_m^e) can be written in terms of the element mass $[M_e]$ matrix as follows:

$$\delta W_m^e = -\int_e \delta w\varrho\ddot{w}\,dx = -\{\delta\vec{q}_w\}_e^T\left(\varrho l_e\int_0^1 [N_s]^T[N_s]\,ds\right)\left\{\ddot{\vec{q}}_w\right\}_e$$

$$= -\{\delta\vec{q}_w\}_e^T [M]_e \left\{ \overrightarrow{\ddot{q}}_w \right\}_e \tag{23}$$

And the external virtual work due to the aerodynamic pressure loading (δW_p) will be:

$$\delta W_p^e = \int_e \delta w p(x) \, \mathrm{d}x = \{\delta\vec{q}_w\}_e^T \left(l_e \int_0^1 [N_s]^T p(s) \, \mathrm{d}s \right) \tag{24}$$

As has been done in the Rayleigh–Ritz approach, the Prandtl–Glauert theory is used for the quasi-steady model. Therefore, the Prandtl's expansion coefficients can be written in terms of the membrane displacement vector $\{\overrightarrow{q}_w\}$ as follows:

$$\begin{Bmatrix} A_o \\ \vdots \\ A_{na} \end{Bmatrix} = \alpha \left\{ \overrightarrow{I_o} \right\} + [\mathcal{P}_s]\{\vec{q}_w\} + \frac{1}{V_\infty}[\mathcal{P}_d]\left\{ \overrightarrow{\dot{q}}_w \right\} \tag{25}$$

The expression of the matrices $[\mathcal{P}_s]$ and $[\mathcal{P}_d]$ is given in Appendix. Substituting Eq. (25) into Eq. (5) and then into Eq. (24) yields an expression for the elemental aerodynamic load vector $\left\{ \overrightarrow{f}_e \right\}$ and the elemental quasi-steady aerodynamic stiffness and damping matrices $[A_s]_e$, $[A_d]_e$ due to the deformation of all elements, which are given in Appendix, as follows:

$$\delta W_p^{\mathcal{QS}} = \{\delta\vec{q}_w\}_e^T \left(q_\infty [A_s]_e \{\vec{q}_w\} + \frac{q_\infty}{V_\infty}[A_d]_e \left\{ \overrightarrow{\dot{q}}_w \right\} + q_\infty \alpha \{\vec{f}_e\} \right) \tag{26}$$

The matrices $[A_s]_e$ and $[A_d]_e$ are of size $2 \times (n_s + 1)$. The finite element formulation of the added-mass pressure coefficient can be written as follows:

$$C_p^{\mathcal{M}}(x^*, k) = -\frac{4ik}{\pi} \int_{-1}^1 \Lambda(x^*, \xi^*) \frac{\overline{w}(\xi^*)}{V_\infty} \, \mathrm{d}\xi^*$$

$$= -\frac{4ik}{\pi} \sum_{j=1}^{ns} \int_{\xi_{1j}^*}^{\xi_{2j}^*} \Lambda(x^*, \xi^*) \left[\left(\frac{ik}{b}[N_s] + \frac{1}{l_{ej}} \frac{\mathrm{d}[N_s]}{\mathrm{d}s} \right) \{\overline{q}_w\}_{ej} - \overline{\alpha} \right] \mathrm{d}\xi^* \tag{27}$$

The membrane nondimensional coordinates (x^*, ξ^*) are related to the elemental coordinates (s, η) as follows:

$$\xi^* = \xi_{1e}^* + \eta \frac{l_e}{b}, \quad x^* = x_{1e}^* + s \frac{l_e}{b} \tag{28}$$

So, the elemental external virtual work of the added-mass pressure $\delta W_p^{\mathcal{M}}$ will be:

$$\delta W_p^{\mathcal{M}} = \int_e \delta w p^{\mathcal{M}}(x) \, \mathrm{d}x = \{\delta\overline{q}_w\}_e^T \left(q_\infty l_e \int_0^1 [N_s]^T C_p^{\mathcal{M}}(x^*, k) \, \mathrm{d}s \right)$$

$$= q_\infty \{\delta\overline{q}_w\}_e^T \left(k^2 [A_{\mathcal{M}1}]_e + ik[A_{\mathcal{M}2}]_e \right) \{\overline{q}_w\} + q_\infty ik\overline{\alpha} \{\delta\overline{q}_w\}_e^T \left\{ f_e^{\mathcal{M}} \right\} \tag{29}$$

Similarly, the external virtual work of the wake term pressure $\delta W_p^{\mathcal{W}}$ will be:

$$\delta W_p^{\mathcal{W}} = \int_e \delta w p^{\mathcal{W}}(x) \, \mathrm{d}x = \{\delta\overline{q}_w\}_e^T \left(q_\infty l_e \int_0^1 [N_w]^T C_p^{\mathcal{W}}(x^*, k) \, \mathrm{d}s \right)$$

$$= q_\infty [1 - C(k)] \{\delta\overline{q}_w\}_e^T \left(ik[A_{\mathcal{W}1}]_e + [A_{\mathcal{W}2}]_e \right) \{\overline{q}_w\} + q_\infty [1 - C(k)]\overline{\alpha} \{\delta\overline{q}_w\}_e^T \left\{ f_e^{\mathcal{W}} \right\} \tag{30}$$

where the elemental matrices $[A_{\mathcal{W}1}]_e$, $[A_{\mathcal{W}2}]_e$, $[A_{\mathcal{M}1}]_e$ and $[A_{\mathcal{M}2}]_e$ are of size $2 x (n_s + 1)$ and their expressions are given in Appendix.

The aerodynamic modeling of a flexible-chord airfoil (without a flap) shown in Fig. 2 is exactly the same as a membrane airfoil except the definition of the shape function which will be than of a flexible beam. So, the nodal displacement vector will contain the nodal rotations besides the nodal translations as $\{\vec{q}_w\}_e = \left\{ w_{1e} \ \theta_{1e} \ w_{2e} \ \theta_{2e} \right\}^T$ and the shape function of the vertical displacement will be as follows:

$$[N_s] = [\, 1 - 3s^2 + 2s^3 \ \ l_e(s - 2s^2 + s^3) \ \ 3s^2 - 2s^3 \ \ l_e(-s^2 + s^3) \,] \tag{31}$$
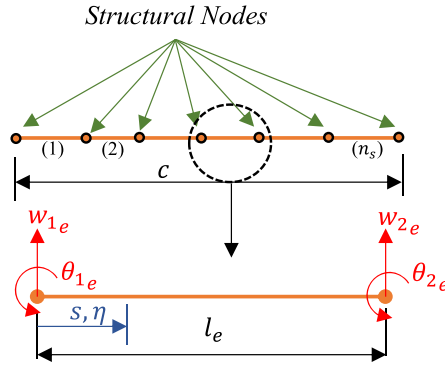
Fig. 4 Finite element discretization of an airfoil

The virtual elastic strain energy of an element can be written of its bending stiffness (EI) follows:

$$\delta U_e = \{\delta \vec{q}_w\}_e^T \left(\frac{EI}{l_e^3} \int_0^1 \frac{\mathrm{d}^2[N_s]^T}{\mathrm{d}s^2} \frac{\mathrm{d}^2[N_s]}{\mathrm{d}s^2}\, \mathrm{d}s \right) \{\vec{q}_w\}_e = \{\delta \vec{q}_w\}_e^T [K]_e \{\vec{q}_w\}_e \qquad (32)$$

The effect of the translation spring (k_w) and the rotational spring (k_ϕ) is simply added to the entries of the stiffness matrix corresponding to the node where the springs are attached. Therefore, the final finite element aeroelastic formulation for a flapless airfoil will be as follows:

$$\mathcal{S}^2 \left([M] + \frac{1}{2}\rho_\infty b^2 [A_{\mathcal{M}1}] \right) \{\vec{q}_w\}_{\mathcal{S}} - \mathcal{S}\frac{q_\infty}{V_\infty}([A_d] + b[A_{\mathcal{M}2}] + b[1 - F(\mathcal{S})][A_{\mathcal{W}1}])\{\vec{q}_w\}_{\mathcal{S}}$$
$$+ ([K] - q_\infty[A_s] - q_\infty[1 - \mathcal{F}(\mathcal{S})][A_{\mathcal{W}2}])\{\vec{q}_w\}_{\mathcal{S}}$$
$$= q_\infty \left(\frac{\mathcal{S}b}{V_\infty} \left\{ \vec{f}^{\mathcal{M}} \right\} + \left\{ \vec{f} \right\} + [1 - \mathcal{F}(\mathcal{S})] \left\{ \vec{f}^{\mathcal{W}} \right\} \right) \alpha \qquad (33)$$

The advantage of the finite element formulation over the Rayleigh–Ritz formulation is that it can be easily extended to model more complex geometries without any reformulations. So, an airfoil with a trailing-edge flap shown in Fig. 3 can be easily modeled by modifying Eq. (33) to be as follows:

$$\mathcal{S}^2 \left([M] + \frac{1}{2}\rho_\infty b^2 [A_{\mathcal{M}1}] \right) \{\vec{q}_w\}_{\mathcal{S}}^{(1)} - \mathcal{S}\frac{q_\infty}{V_\infty}([A_d] + b[A_{\mathcal{M}2}] + b[1 - F(\mathcal{S})][A_{\mathcal{W}1}])\{\vec{q}_w\}_{\mathcal{S}}^{(1)}$$
$$+ ([K] - q_\infty[A_s] - q_\infty[1 - \mathcal{F}(\mathcal{S})][A_{\mathcal{W}2}])\{\vec{q}_w\}_{\mathcal{S}}^{(1)}$$
$$= q_\infty \left(\frac{\mathcal{S}b}{V_\infty} \left\{ \vec{f}^{\mathcal{M}} \right\} + \left\{ \vec{f} \right\} + [1 - \mathcal{F}(\mathcal{S})] \left\{ \vec{f}^{\mathcal{W}} \right\} \right) \alpha$$
$$+ \left(\mathcal{S}^2 \left\{ \vec{f}_\beta^{\mathcal{M}} \right\} + \mathcal{S}\frac{q_\infty}{V_\infty} \left\{ \vec{f}_\beta^D \right\} + q_\infty \left\{ \vec{f}_\beta^S \right\} \right) \beta \qquad (34)$$

The aerodynamic force vectors due to the flap deflection $\left\{ \vec{f}_\beta^{\mathcal{M}} \right\}$, $\left\{ \vec{f}_\beta^D \right\}$, and $\left\{ \vec{f}_\beta^S \right\}$ can be easily computed from the aerodynamic matrices using the principle of superposition such that the total airfoil deformation can be decomposed into two components; the first component is the undeformed airfoil with a unit flap deflection angle $\{\vec{q}_w\}^{(o)}$, and the second component is the deformed airfoil without a flap deflection $\{\vec{q}_w\}^{(1)}$. Therefore, the flap aerodynamic force vectors are as follows:

$$\left\{ \vec{f}_\beta^{\mathcal{M}} \right\} = -\frac{1}{2}\rho_\infty b^2 [A_{\mathcal{M}1}]\{\vec{q}_w\}^{(o)}$$
$$\left\{ \vec{f}_\beta^D \right\} = ([A_d] + b[A_{\mathcal{M}2}] + b[1 - F(\mathcal{S})][A_{\mathcal{W}1}])\{\vec{q}_w\}^{(o)}$$
$$\left\{ \vec{f}_\beta^S \right\} = ([A_s] + [1 - \mathcal{F}(\mathcal{S})][A_{\mathcal{W}2}])\{\vec{q}_w\}^{(o)} \qquad (35)$$
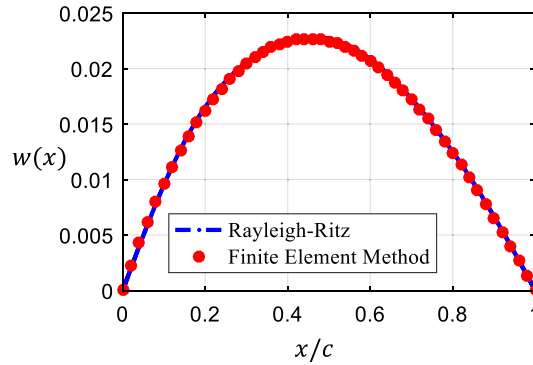
Fig. 5 The static deflection shape of the membrane airfoil due to an initial angle of attack ($\alpha = 3$, $C_T = 3$)

Table 1 Verification of the present FEM and the Rayleigh–Ritz method for a membrane airfoil

Static analysis ($\alpha = 3^o$, $C_T = 3$)							
Method	C_L	$C_{L\alpha}$	C_M	C_{MLE}	$x_{cp}/c\%$	$z_{cmax}/c\%$	$V_D(m/s)$
FEM	0.577	11.02	-0.0580	-0.2022	35.04	2.27	19.8
Rayleigh–Ritz	0.577	11.02	-0.0580	-0.2022	35.04	2. 27	19.8
Nielsen [8]	0.570	10.90	–	–	35.42	2.27	19.8
Lift coefficient convergence study							
No. of elements (Modes)	10 (1)	20 (3)	25 (5)	30 (7)	40 (9)	45 (11)	50 (13)
FEM	0.5712	0.5757	0.5763	0.5766	0.5770	0.5770	0.5771
Rayleigh–Ritz	0.6017	0.5817	0.5791	0.5782	0.5779	0.5777	0.5776
Flutter speed analysis ($\varrho/\rho_\infty c = 25$)							
FEM			Rayleigh–Ritz	Tiomkin [17]			
14.7 m/s			14.5 m/s	14.3 m/s			

4 Numerical results

4.1 Membrane airfoils

The aeroelastic formulations and codes are verified by considering a membrane airfoil with a chord (c) length of 1 m and a mass per unit (ϱ) of 0.5 kg/m. The membrane is subjected to a free stream with air density (ρ_∞) of 1.225 kg/m^3 and speed (V_∞) of 15 m/s at an angle of attack (α) of 3 degrees and an applied tension force coefficient ($C_T = T/q_\infty c$) of 3. For the Rayleigh–Ritz approach, 20 terms were considered for the membrane deformation, while for the FEM 50 elements were considered for the study and 40 aerodynamic terms were used for the Prandtl–Glauert series expansion. The static deformation shape of the membrane airfoil is shown in Fig. 5, and the values of the corresponding aerodynamic coefficients (the lift coefficient (C_L), the lift-alpha curve slope ($C_{L\alpha}$), the moment coefficient at the quarter chord (C_M), the leading-edge moment coefficient (C_{MLE}), the center of pressure (x_{cp}), the maximum camber (z_{cmax}), and the divergence speed (V_D)) are presented in Table 1, and it can be seen that both the Rayleigh–Ritz and the FEM are in a good agreement with results of Nielsen [8].

Modal analysis was used for the dynamic analysis of the membrane airfoil. The first four mode shapes obtained from the FEM are shown in Fig. 6. Only heavy membranes exhibit flutter instability, so the membrane density ratio ($\varrho/\rho_\infty c$) is set to 25 and the root loci of the dynamic system as the free stream speed increases from 0 to 18 m/s are computed as shown in Fig. 7. It can be seen that the system becomes dynamically unstable at speed of 14.5 m/s which is corresponding to a tension coefficient of 3.2 and it is the value reported by Tiomkin [17]. All modes exhibit reduction in their frequencies as the speed increases due to the loss of stiffness caused by the aerodynamic loading. Regarding the computational cost of each method, the two codes were written in Matlab and run on a Intel(R) Core(TM) i7-10870H CPU @ 2.20 GHz Machine. The time required to get the final dynamic aeroelastic system using the Rayleigh–Ritz (20 terms) method and the finite element method (50 elements) was 0.61 and 10.5 s, respectively, which is a significant difference, but as the geometrical complexity of the problem increases, the Rayleigh–Ritz will no longer be suitable. The running time of the finite element
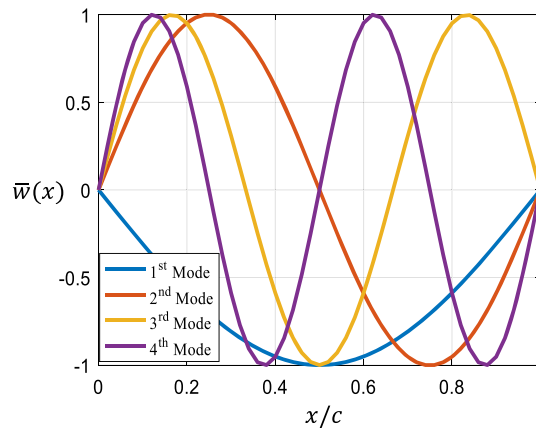
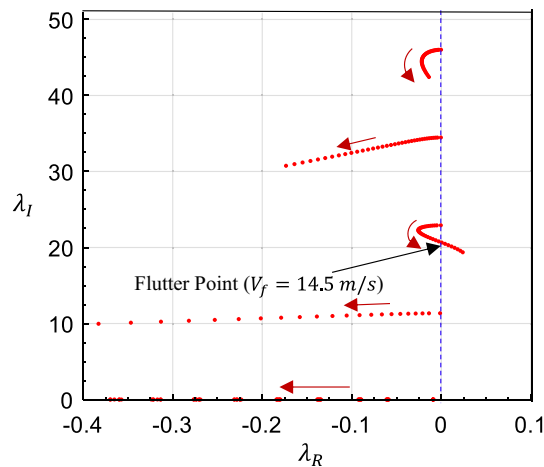**Fig. 6** The first four normalized natural mode shapes of membrane airfoil using the FEM

Fig. 7 Root loci of the heavy membrane airfoil ($\varrho/\rho_\infty c = 25$) for the free stream speed range 0–18 m/s

code can be reduced by using less number of elements and by utilizing parallel processing techniques which will be considered in the future.

The aeroelastic characteristics of a membrane airfoil with a TE flap are studied by considering a membrane with the same properties mentioned earlier. The TE flap is modeled by a single element in case of the FEM. Table 2 shows a parametric analysis for different flap lengths and combinations of the angle of attack and the flap deflection angle. Figure 8 shows the deformation shape of the membrane airfoil with/without flap deflection at a 3° angle of attack. The maximum camber shifts toward the LE for an upward flap deflection and vice versa for a downward flap deflection. Also, an inflection point appears near the TE for an upward flap deflection. Figures 9 and 10 show the variation of the lift and moment coefficient with the TE flap length for different tension coefficient values. Both the lift and moment coefficients exhibit nonlinear relations in terms of the flap length and the tension coefficient. The moment shows stronger nonlinearity compared to the lift and as the tension coefficient increases, this nonlinearity decreases.

The dynamic aeroelastic characteristics of the membrane airfoil are studied by considering the transient response due to a step and harmonic flap deflections using eight natural mode shapes. Figures 11 and 12 show the step response of the lift and moment coefficients, while Figs. 13, 14, 15, and 16 show the first four modes step responses. The higher modes have low aerodynamic damping leading to the superharmonics in the coefficients' step responses which can be eliminated by adding structural damping. The frequency response due to harmonic TE flap deflection is shown in Figs. 17, 18, and 19. Initially, as the reduced frequency increases, the lift coefficient amplitude decreases due to the influence of the wake; then, it increases as the reduced frequency approaches the aeroelastic natural frequency of the membrane. As the flap length and the tension coefficient increase, the peak lift amplitude increases relative to static values.
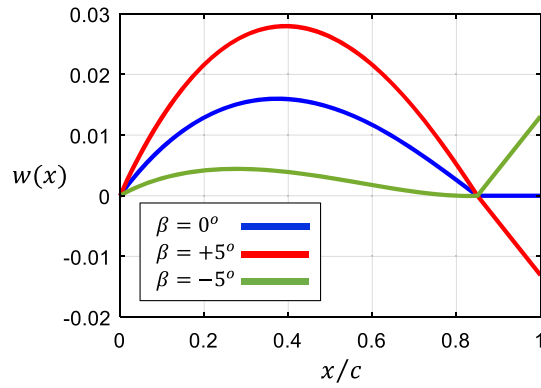
Fig. 8 The deflection shape of the membrane airfoil with a TE flap ($\alpha = 3°$, $C_T = 3$, $e = 0.15$)
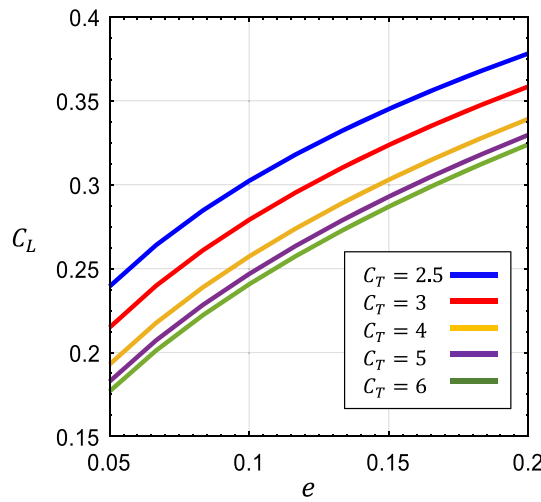
Fig. 9 The variation of the static lift coefficient of the membrane airfoil with the TE flap length ($\beta = 5°$, $\alpha = 0^o$)
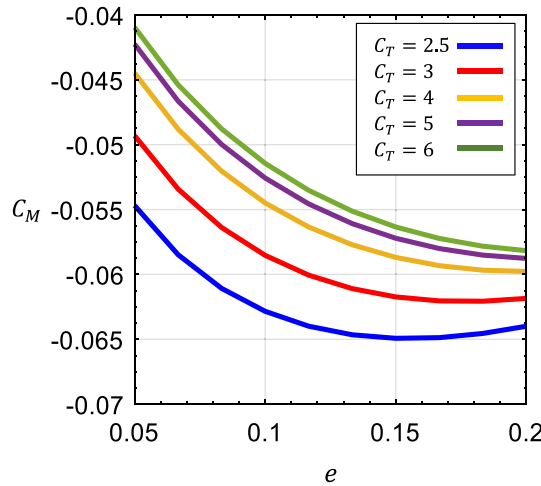

Fig. 10 The variation of the static moment coefficient of the membrane airfoil with the TE flap length ($\beta = 5°$, $\alpha = 0^o$)

Table 2 Aerodynamics parameters of the membrane airfoil for different combinations of the TE flap deflection angle, the angle of attack and the TE flap length

Flap length (e) %	α^o	β^o	C_L	$C_{L\alpha}$	$C_{Mc/4}$	C_{MLE}	$x_{cp}/c\%$	$z_{cmax}/c\%$
5	0	+ 5	0.2149	–	− 0.0493	− 0.1030	47.94	0.82
	3	0	0.4468	8.53	− 0.0224	− 0.1340	30	1.77
	3	+ 5	0.6617	12.63	− 0.0717	− 0.2371	35.83	2.59
	3	− 5	0.2319	4.43	0.0269	− 0.0310	13.38	0.96
10	0	+ 5	0.2791	–	− 0.0585	− 0.1283	45.97	1.06
	3	0	0.4206	8.03	− 0.0139	− 0.1191	28.31	1.67
	3	+ 5	0.6997	13.36	− 0.0725	− 0.2474	35.36	2.71
	3	− 5	0.1416	2.704	0.0446	0.0092	− 0.065	0.87
15	0	+ 5	0.3236	–	− 0.0617	− 0.1426	44.08	1.21
	3	0	0.4050	7.73	− 0.0086	− 0.1098	27.13	1.60
	3	+ 5	0.7285	13.91	− 0.0703	− 0.2525	34.66	2.8
	3	− 5	0.0814	1.554	0.0531	0.0328	− 0.4029	1.31
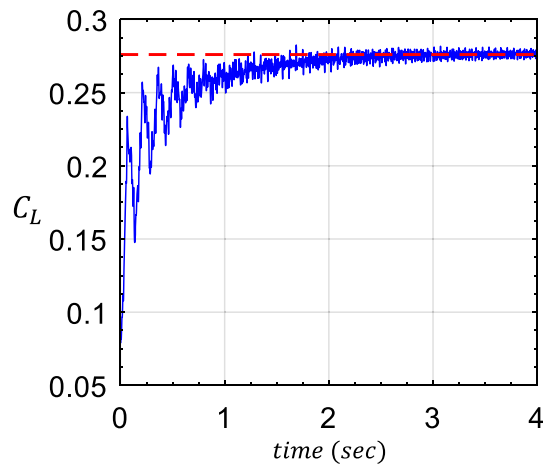
Fig. 11 The lift coefficient time response of the membrane airfoil due to a step TE flap deflection ($\beta = 5°$, $C_T = 3$, $e = 0.1$)
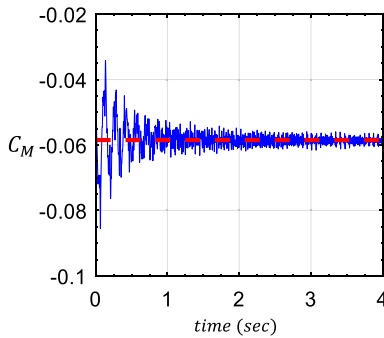
Fig. 12 The moment coefficient time response of the membrane airfoil due to a step TE flap deflection ($\beta = 5°$, $C_T = 3$, $e = 0.1$)

4.2 Flexible-chord airfoils

This section investigates the aeroelastic characteristics of deformable airfoils. The considered airfoil has a unit chord length and mass per unit length (ϱ) of 4 kg/m. The free stream flow has an air density (ρ_∞) of 1.225 kg/m^3 and speed (V_∞) of 15 m/s at an angle of attack (α) of 3 degrees. The airfoil flexibility is represented by the nondimensional bending stiffness ($\overline{EI} = EI/q_\infty c^4$) which is set to vary from 0.5 to infinity. The torsional and translational spring constants ($k_\varnothing$, k_w) are set to 800 N.m/rad. For the dynamic analysis, the translational spring constant is set to be equal to the torsional spring constant ($k_w = k_\varnothing$) and for the static analysis $k_w = 10k_\varnothing$ as it has no contribution to the results which will be more appropriate for deformation demonstration purposes.
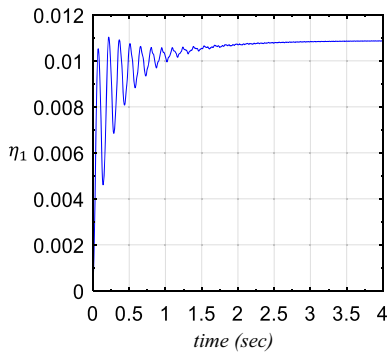
Fig. 13 The time response of the first mode of the membrane airfoil due to a step TE flap deflection ($\beta = 5°$, $C_T = 3$, $e = 0.1$)
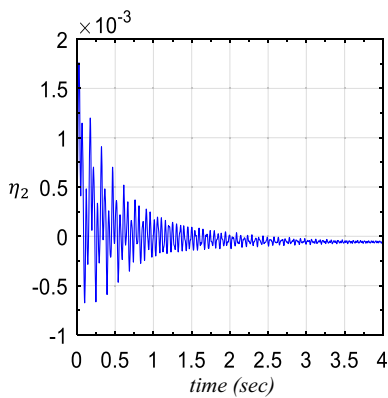
Fig. 14 The time response of the second mode of the membrane airfoil due to a step TE flap deflection ($\beta = 5°$, $C_T = 3$, $e = 0.1$)
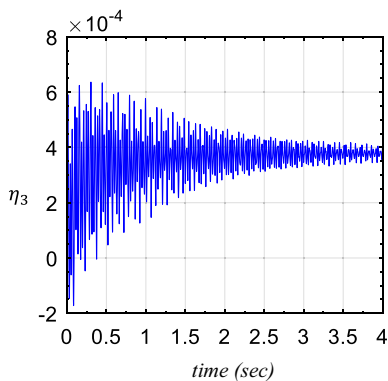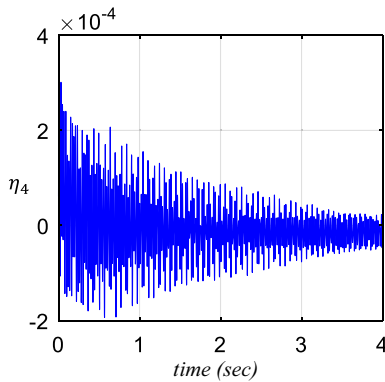

Fig. 15 The time response of the third mode of the membrane airfoil due to a step TE flap deflection ($\beta = 5°$, $C_T = 3$, $e = 0.1$)

The TE flap stiffness constant (k_J) is set to be very large such that the flap deflection angle does not change by the flap deformation. The airfoil is discretized into 60 elements in the case of the FEM, and 20 basis functions are used in the case of the Rayleigh–Ritz method.

Static aeroelastic analysis is initially performed for zero flap angle and $3°$ initial angle of attack using the FEM and the Rayleigh–Ritz method which yielded identical results. Figures 20, 21, and 22 show the deformation shape, the lift coefficient, and the moment coefficient for different rigid-body springs position (x_s), respectively. As the spring position moves forward toward the LE, the TE part suffers more deformation which lead to lift force loss till it drops below the rigid-airfoil values. The effect of the airfoil flexibility on the aerodynamic coefficients strongly depends on the springs position, as this effect decreases as the springs position moves forward. For the flutter speed analysis shown in Fig. 23, the airfoil flexibility in general decreases the flutter speed compared to the rigid airfoil and this effect increases as x_s moves toward the LE. It

Fig. 16 The time response of the fourth mode of the membrane airfoil due to a step TE flap deflection ($\beta = 5°$, $C_T = 3$, $e = 0.1$)
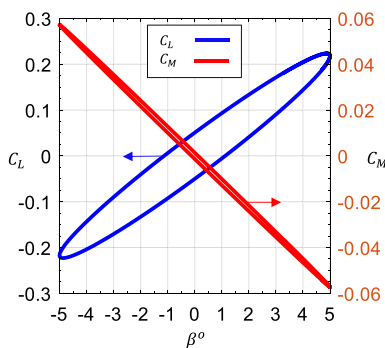
Fig. 17 The lift and moment coefficients variations cycles of the membrane airfoil due to a harmonic TE flap deflection ($\beta = 5°$, $C_T = 3$, $e = 0.1$, $k = 0.1$)
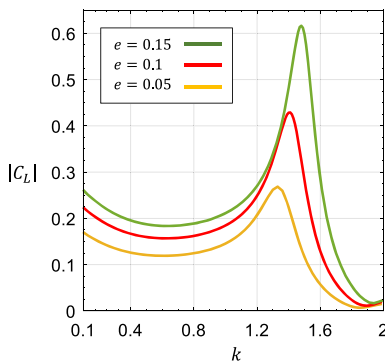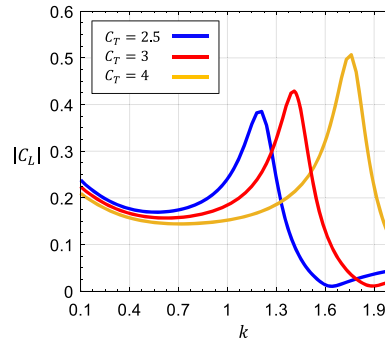

Fig. 18 The lift coefficient frequency response of the membrane airfoil due to a harmonic TE flap deflection for different flap lengths ($\beta = 5°$, $C_T = 3$)

seems that for certain x_s positions and flexibility levels, flexibility can increase the flutter speed as in the case of $\overline{EI} = 0.5$ and $x_s/c > 0.49$.

The effect of the TE flap deflection angle is shown in Figs. 24, 25, 26, 27 and 28. The airfoil flexibility has less effect on the lift coefficient compared to the moment coefficient, and it can completely vanish for certain rigid-body springs position as shown in Fig. 27 which shows no flexibility effect on the lift coefficient for $x_s/c \approx 0.53$. The aerodynamic coefficients transient responses due to a step TE flap input are shown in Figs. 29 and 30. Compared to membrane airfoils, higher modes seem to have less influence on the coefficient responses. Figures 31 and 32 show the lift and moment coefficients cycles due to a harmonic TE flap input at a reduced frequency of 0.1 for $x_s = 0.5$and0.3, respectively, while Figs. 33 and 34 show the frequency responses. As the reduced frequency increases, the amplitude decreases due to wake effect and due to the interaction with the plunging mode till it almost vanishes at a reduced frequency of 0.46; then, it increases to

Fig. 19 The lift coefficient frequency response of the membrane airfoil due to a harmonic TE flap deflection for different tension coefficients ($\beta = 5°$, $e = 0.1$)
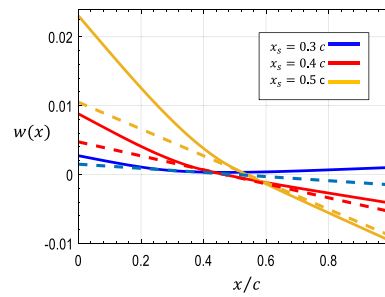
Fig. 20 The deformation shape of the flexible-chord airfoil for different rigid-body springs positions ($\overline{EI} = 1$, $\alpha = 3°$). Flexible airfoil (solid lines), rigid airfoils (dashed lines)
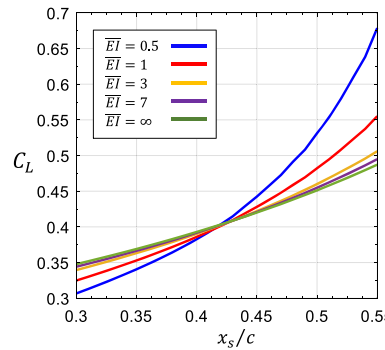

Fig. 21 The variation of the static lift coefficient of the flexible-chord airfoil with the position of the rigid-body springs due to an initial angle of attack ($\alpha = 3°$)
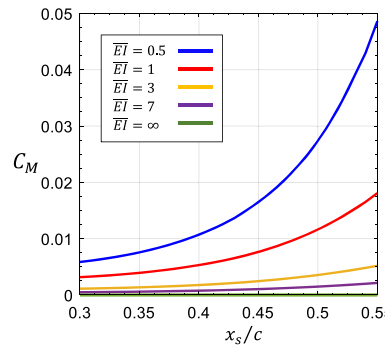
Fig. 22 The variation of the static moment coefficient of the flexible-chord airfoil with the position of the rigid-body springs due to an initial angle of attack ($\alpha = 3°$)
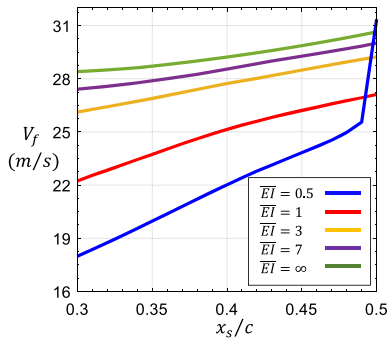
Fig. 23 The variation of the flutter speed of the flexible-chord airfoil with the position of the rigid-body springs ($k_\varnothing/k_w = 1$)
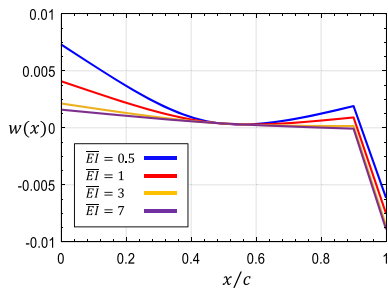
Fig. 24 The deformation shape of the flexible-chord airfoil due to a TE flap deflection ($\beta = 5°$, $x_s/c = 0.5$, $\alpha = 0°$)
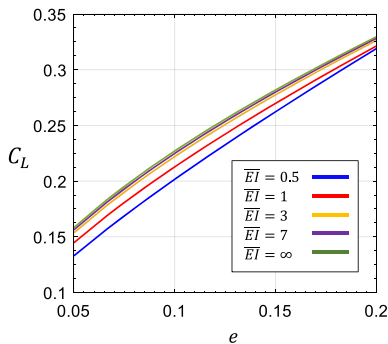
Fig. 25 The variation of the static lift coefficient of the flexible-chord airfoil with the TE flap length ($\beta = 5°$, $x_s/c = 0.5$, $\alpha = 0°$)

the peak value at the first bending mode aeroelastic natural frequency. The peak amplitude increases as the springs position moves forward.

5 Conclusion

The aeroelastic performances of membrane airfoils and flexible-chord airfoils with TE flaps are studied in this paper. Two aeroelastic formulations are presented; the Rayleigh–Ritz formulation and the finite element formulation. The two presented formulations are very efficient as the fluid–structure interactions are presented in closed-form, easy to compute, aerodynamic matrices. The finite element formulation has the advantage of modeling complex geometries without any adjustments to its formulation, so it is more suitable to model flapped airfoils. The analysis of both airfoil types showed that the aerodynamic moment coefficient is more sensitive to the flexibility level and to the TE flap length. For flexible-chord airfoils, the position of the elastic axis (the rigid-body springs position) plays a major role in the effect of the flexibility on the aeroelastic characteristics. The flutter speed decreases with increased airfoil flexibility, except for certain elastic axis positions of flexible-chord airfoils where the flexibility increases the flutter speed. For harmonic TE flap input, the peak amplitude
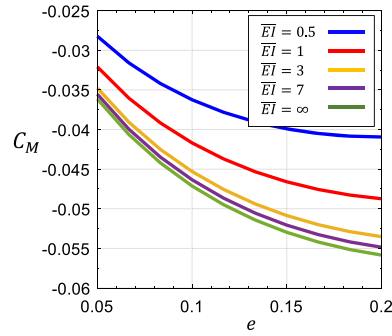
Fig. 26 The variation of the static moment coefficient of the flexible-chord airfoil with the TE flap length ($\beta = 5°$, $x_s/c = 0.5$, $\alpha = 0°$)
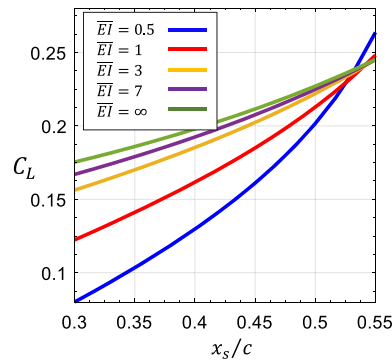

Fig. 27 The variation of the static lift coefficient of the flexible-chord airfoil with the position of the rigid-body springs due to a TE flap deflection ($\beta = 5°$, $e = 0.1$)
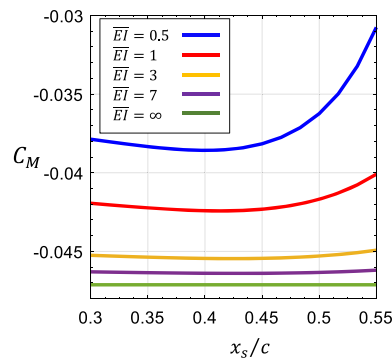

Fig. 28 The variation of the static moment coefficient of the flexible-chord airfoil with the position of the rigid-body springs due to a TE flap deflection ($\beta = 5°$, $e = 0.1$)
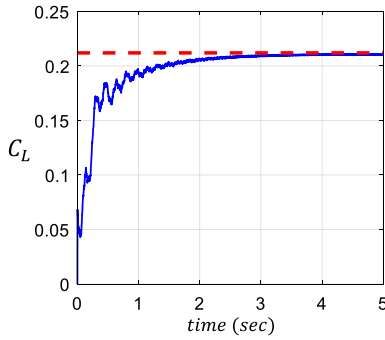
Fig. 29 The lift coefficient time response of the flexible-chord airfoil due to a step TE flap deflection ($\beta = 5°$, $\overline{EI} = 1$, $x_s/c = 0.5$)
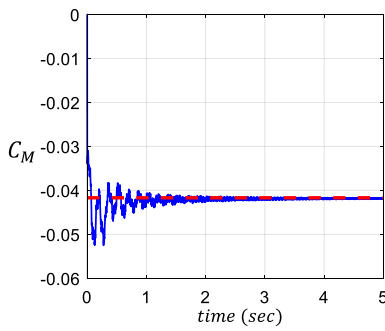

Fig. 30 The moment coefficient time response of the flexible-chord airfoil due to a step TE flap deflection ($\beta = 5°$, $\overline{EI} = 1$, $x_s/c = 0.5$)
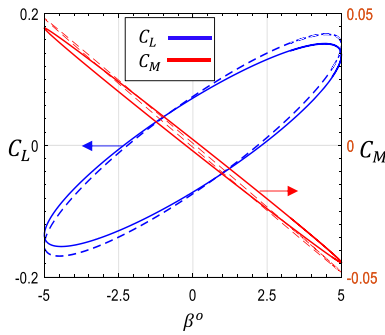

Fig. 31 The lift and moment coefficients variations cycles of the flexible-chord airfoil due to a harmonic TE flap deflection ($\beta = 5°$, $\overline{EI} = 1$, $x_s/c = 0.5$, $k = 0.1$). Flexible airfoil (solid lines), rigid airfoil (dashed lines)

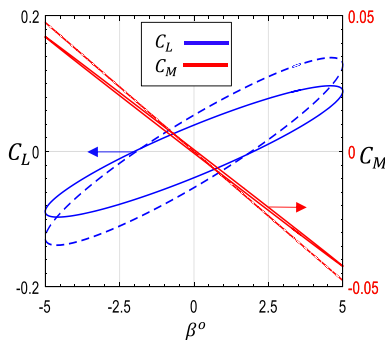**Fig. 32** The lift and moment coefficients variations cycles of the flexible-chord airfoil due to a harmonic TE flap deflection ($\beta = 5°$, $\overline{EI} = 1$ $x_s/c = 0.3$, $k = 0.1$). Flexible airfoil (solid lines), rigid airfoil (dashed lines)
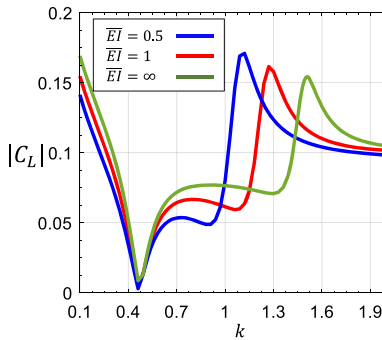
Fig. 33 The lift coefficient frequency response of the flexible-chord airfoil due to a harmonic TE flap deflection ($\beta = 5°$, $x_s/c = 0.5$, $e = 0.1$)
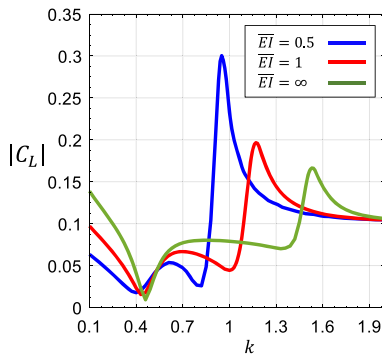

Fig. 34 The lift coefficient frequency response of the flexible-chord airfoil due to a harmonic TE flap deflection ($\beta = 5°$, $x_s/c = 0.3$, $e = 0.1$)

of the aerodynamic coefficients increases with the flexibility level, flap length and as the elastic axis moves forward.

Declarations

Conflict of interest The author declares no conflict of interests of any kind.

Appendix

Rayleigh–Ritz formulation

$$[M] = \frac{\varrho c}{2}[I], \quad [K] = \frac{T}{2c}\begin{bmatrix} (\pi)^2 & 0 & & \dots & 0 \\ 0 & (2\pi)^2 & \dots & & \vdots \\ \vdots & & \ddots & & 0 \\ 0 & \dots & & 0 & (N_s\pi)^2 \end{bmatrix} \tag{A.1}$$

$$\mathcal{A}(m,n) = \frac{\mathcal{C}^{(m)}}{\pi} \int_0^\pi \varphi_{n,x}(x) \cos(m\theta)\, \mathrm{d}\theta \tag{A.2}$$

$$\mathcal{B}(m,n) = \frac{\mathcal{C}^{(m)}}{\pi} \int_0^\pi \varphi_n(x) \cos(m\theta)\, \mathrm{d}\theta, \quad \mathcal{C}^{(m)} = \begin{cases} -1 & m=0 \\ 2 & m \neq 0 \end{cases} \tag{A.3}$$

$$\mathcal{D}(n,\,:) = \int_0^c \left\lfloor \frac{1+\cos(\theta)}{\sin(\theta)} \ \sin(\theta) \ \sin(2\theta) \ \ldots \ \sin(n_a\theta) \right\rfloor \varphi_n(x)\, \mathrm{d}x \tag{A.4}$$

$$[A_s] = 4[\mathcal{D}][\mathcal{A}], \quad [A_d] = 4[\mathcal{D}][\mathcal{B}], \quad \left\{\vec{f}\right\} = 4[\mathcal{D}]\left\{\vec{I_o}\right\} \tag{A.5}$$

$$C(k) = \frac{H_1^{(2)}}{H_1^{(2)} + i\,H_0^{(2)}}, \Lambda\big(x^*,\xi^*\big) = \frac{1}{2}\ln\frac{1-x^*\xi^* + \sqrt{\big(1-x^{*2}\big)\big(1-\xi^{*2}\big)}}{1-x^*\xi^* - \sqrt{\big(1-x^{*2}\big)\big(1-\xi^{*2}\big)}} \tag{A.6}$$

$$A_{\mathcal{M}1}(n,l) = \frac{4}{\pi} \int_{-1}^1 \int_{-1}^1 \varphi_n(x^*) \Lambda(x^*,\xi^*) \varphi_l(\xi^*)\, \mathrm{d}\xi^* \mathrm{d}x^* \tag{A.7}$$

$$A_{\mathcal{M}2}(n,l) = -\frac{4b}{\pi} \int_{-1}^1 \int_{-1}^1 \varphi_n(x^*) \Lambda(x^*,\xi^*) \varphi_{l,\xi}(\xi^*)\, \mathrm{d}\xi^* \mathrm{d}x^* \tag{A.8}$$

$$\left\{\vec{f}^{\mathcal{M}}\right\} = \frac{4b}{\pi} \int_{-1}^1 \int_{-1}^1 \varphi_n(x^*) \Lambda(x^*,\xi^*)\, \mathrm{d}\xi^* \mathrm{d}x^* \tag{A.9}$$

$$A_{\mathcal{W}1}(n,l) = \frac{4}{\pi} \int_{-1}^1 \int_{-1}^1 \varphi_n(x^*) \sqrt{\frac{1-x^*}{1+x^*}} \sqrt{\frac{1+\xi^*}{1-\xi^*}} \varphi_l(\xi^*)\, \mathrm{d}\xi^* \mathrm{d}x^* \tag{A.10}$$

$$A_{\mathcal{W}2}(n,l) = \frac{4b}{\pi} \int_{-1}^1 \int_{-1}^1 \varphi_n(x^*) \sqrt{\frac{1-x^*}{1+x^*}} \sqrt{\frac{1+\xi^*}{1-\xi^*}} \varphi_{l,\xi}(\xi^*)\, \mathrm{d}\xi^* \mathrm{d}x^* \tag{A.11}$$

$$\left\{\vec{f}^{\mathcal{W}}\right\} = \frac{-4b}{\pi} \int_{-1}^1 \int_{-1}^1 \varphi_n(x^*) \sqrt{\frac{1-x^*}{1+x^*}} \sqrt{\frac{1+\xi^*}{1-\xi^*}}\, \mathrm{d}\xi^* \mathrm{d}x^* \tag{A.12}$$

Finite element formulation

$$\mathcal{P}_s(m,j) = \frac{\mathcal{C}^{(m)}}{\pi} \frac{1}{l_{ej}} \int_{\theta_{j1}}^{\theta_{j2}} \left(\frac{d[N_s]}{ds}\right) \cos(m\theta)\mathrm{d}\theta \tag{A.13}$$

$$\mathcal{P}_d(m,j) = \frac{\mathcal{C}^{(m)}}{\pi} \int_{\theta_{j1}}^{\theta_{j2}} [N_s] \cos(m\theta)\mathrm{d}\theta, \ \mathcal{C}^{(m)} = \begin{cases} -1 & m=0 \\ 2 & m \neq 0 \end{cases} \tag{A.14}$$

$$[A_s]_e = 4l_e \int_0^1 [N_s]^T \left\lfloor \frac{1+\cos(\theta)}{\sin(\theta)} \ \sin(\theta) \ \ldots \ \sin(n_a\theta) \right\rfloor [\mathcal{P}_s]\mathrm{d}s \tag{A.15}$$

$$[A_d]_e = 4l_e \int_0^1 [N_s]^T \left\lfloor \frac{1+\cos(\theta)}{\sin(\theta)} \ \sin(\theta) \ \ldots \ \sin(n_a\theta) \right\rfloor [\mathcal{P}_d]\mathrm{d}s \tag{A.16}$$

$$\{f_e\} = 4l_e \int_0^1 [N_s]^T \frac{1+\cos(\theta)}{\sin(\theta)}\mathrm{d}s \tag{A.17}$$

$$[A_{\mathcal{M}1}]_e\{\overline{q}_w\} = \frac{4l_e}{\pi b^2} \sum_{j=1}^{ns} l_{ej} \int_0^1 \int_0^1 [N_s]^T \Lambda(x^*,\xi^*) N_\eta \{\overline{q}_w\}_{ej}\, \mathrm{d}s\, \mathrm{d}\eta \tag{A.18}$$

$$[A_{\mathcal{M}2}]_e\{\overline{q}_w\} = -\frac{4l_e}{\pi b} \sum_{j=1}^{ns} \int_0^1 \int_0^1 [N_s]^T \Lambda(x^*,\xi^*) \frac{dN_\eta}{d\eta} \{\overline{q}_w\}_{ej}\, ds d\eta \tag{A.19}$$

$$\left\{f_e^{\mathcal{M}}\right\} = \frac{4l_e}{\pi b} \sum_{j=1}^{ns} l_{ej} \int_0^1 \int_0^1 [N_s]^T \Lambda(x^*,\xi^*)\, \mathrm{d}s\, \mathrm{d}\eta \tag{A.20}$$

$$[A_{\mathcal{W}1}]_e\{\overline{q}_w\} = \frac{4l_e}{\pi b^2} \sum_{j=1}^{ns} l_{ej} \int_0^1 \int_0^1 [N_s]^T \sqrt{\frac{1-x^*}{1+x^*}} \sqrt{\frac{1+\xi^*}{1-\xi^*}} N_\eta \{\overline{q}_w\}_{ej}\, \mathrm{d}s\, \mathrm{d}\eta \tag{A.21}$$

$$[A_{\mathcal{W}2}]_e\{\overline{q}_w\} = \frac{4l_e}{\pi b} \sum_{j=1}^{ns} \int_0^1 \int_0^1 [N_s]^T \sqrt{\frac{1-x^*}{1+x^*}} \sqrt{\frac{1+\xi^*}{1-\xi^*}} \frac{dN_\eta}{d\eta} \{\overline{q}_w\}_{ej}\, \mathrm{d}s\, \mathrm{d}\eta \tag{A.22}$$

$$\left\{f_e^{\mathcal{W}}\right\} = \frac{-4l_e}{\pi b} \sum_{j=1}^{ns} l_{ej} \int_0^1 \int_0^1 [N_s]^T \sqrt{\frac{1-x^*}{1+x^*}} \sqrt{\frac{1+\xi^*}{1-\xi^*}}\, \mathrm{d}s\, \mathrm{d}\eta \tag{A.23}$$

References

1. Woods, B.K., Friswell, M.I.: Structural Characterization of the fish bone active camber morphing airfoil. In: 22nd AIAA/ASME/AHS Adaptive Structures Conference. American Institute of Aeronautics and Astronautics, National Harbor, Maryland (2014)
2. Taylor, G.I.: On the shapes of parachutes. Scientific papers of G.I.T. III, 26–37 (1919)
3. Warner, E.P.: The aerodynamics of yacht sails. Massachusetts Institute of Technology, Aeronautical Engineering, Read at the 33rd general meeting of the Society of Naval Architects and Marine Engineers, SNAME, New York, USA. (1925)
4. Newman, B.G.: Aerodynamic theory for membranes and sails. Prog. Aerosp. Sci. **24**, 1–27 (1987). https://doi.org/10.1016/0376-0421(87)90005-4
5. Newman, B.G.: The aerodynamics of flexible membranes. 24
6. Tiomkin, S., Raveh, D.E.: A review of membrane-wing aeroelasticity. Prog. Aerosp. Sci. **126**, 100738 (2021). https://doi.org/10.1016/j.paerosci.2021.100738
7. Thwaites, B., Temple, G.F.J.: The aerodynamic theory of sails. I. Two-dimensional sails. Proc. R. Soc. Lond. Ser. A Math. Phys. Sci. **261**, 402–422 (1961). https://doi.org/10.1098/rspa.1961.0086
8. Nielsen, J.N.: Theory of flexible aerodynamic surfaces. J. Appl. Mech. **30**, 435–442 (1963). https://doi.org/10.1115/1.3636575
9. Jackson, P.S.: A simple model for elastic two-dimensional sails. AIAA J. **21**, 153–155 (1983). https://doi.org/10.2514/3.60106
10. Newman, B.G., Low, H.T.: Two-dimensional impervious sails: experimental results compared with theory. J. Fluid Mech. **144**, 445–462 (1984)
11. Greenhalgh, S., Curtiss, H.C., Smith, B.: Aerodynamic properties of a two-dimensional inextensible flexible airfoil. AIAA J. **22**, 865–870 (1984). https://doi.org/10.2514/3.8701
12. Newman, B.G., Païdoussis, M.P.: The stability of two-dimensional membranes in streaming flow. J. Fluids Struct. **5**, 443–454 (1991). https://doi.org/10.1016/0889-9746(91)90437-T
13. Mavroyiakoumou, C., Alben, S.: Eigenmode analysis of membrane stability in inviscid flow. Phys. Rev. Fluids **6**, 043901 (2021). https://doi.org/10.1103/PhysRevFluids.6.043901
14. Mavroyiakoumou, C., Alben, S.: Large-amplitude membrane flutter in inviscid flow. J. Fluid Mech. **891**, A23 (2020). https://doi.org/10.1017/jfm.2020.153
15. Saffman, P.G.: Vortex Dynamics. Cambridge University Press, Cambridge (1993)
16. Sygulski, R.: Stability of membrane in low subsonic flow. Int. J. Non-Linear Mech. **42**, 196 (2007). https://doi.org/10.1016/j.ijnonlinmec.2006.11.012
17. Tiomkin, S., Raveh, D.E.: On the stability of two-dimensional membrane wings. J. Fluids Struct. **71**, 143–163 (2017). https://doi.org/10.1016/j.jfluidstructs.2017.03.003
18. Alon Tzezana, G., Breuer, K.: Thrust, drag and wake structure in flapping compliant membrane wings. J. Fluid Mech. **862**, 871–888 (2019). https://doi.org/10.1017/jfm.2018.966
19. Wu, T.Y.-T.: Swimming of a waving plate. J. Fluid Mech. **10**, 321–344 (1961). https://doi.org/10.1017/S0022112061000949
20. Hussein, O.S.: Nonlinear FE aeroelastic analysis of membrane airfoils with fixed and elastic supports. Thin-Walled Struct. (2023). https://doi.org/10.1016/j.tws.2023.110544
21. Serrano Galiano, S., Sandberg, R.D.: Effect of the leading and trailing edge geometry on the fluid-structural coupling of membrane aerofoils. In: 54th AIAA Aerospace Sciences Meeting. American Institute of Aeronautics and Astronautics (2016)
22. Smith, R., Shyy, W.: Computational model of flexible membrane wings in steady laminar flow. AIAA J. **33**, 1769–1777 (1995). https://doi.org/10.2514/3.12811
23. Tiomkin, S., Raveh, D.: On membrane-wing stability in laminar flow. J. Fluids Struct. **91**, 102694 (2019). https://doi.org/10.1016/j.jfluidstructs.2019.102694
24. Tiomkin, S., Raveh, D.: Membrane wing dynamic stability: the role of membrane mass. Presented at the AIAA SciTech, Forum January 8 (2018)
25. Sun, X., Ren, X.-L., Zhang, J.-Z.: Nonlinear dynamic responses of a perimeter-reinforced membrane wing in laminar flows. Nonlinear Dyn. **88**, 749–776 (2017). https://doi.org/10.1007/s11071-016-3274-3
26. Su, W.: Development of an aeroelastic formulation for deformable airfoils using orthogonal polynomials. AIAA J. (2017)
27. Johnson, M., Peters, D.A.: Finite-State airloads for deformable airfoils on fixed and rotating wings. In: Proceedings of Symposium on Aeroelasticity and Fluid Structure Interaction Problems, pp. 1–28. New York (1994)
28. Walker, W.P., Patil, M.J.: Unsteady Aerodynamics of deformable thin airfoils
29. Murua, J., Palacios, R., Peiró, J.: Camber effects in the dynamic aeroelasticity of compliant airfoils. J. Fluids Struct. **26**, 527–543 (2010). https://doi.org/10.1016/j.jfluidstructs.2010.01.009
30. Berci, M., Gaskell, P.H., Hewson, R.W., Toropov, V.V.: A semi-analytical model for the combined aeroelastic behaviour and gust response of a flexible aerofoil. J. Fluids Struct. **38**, 3–21 (2013). https://doi.org/10.1016/j.jfluidstructs.2012.11.004
31. Riso, C., Riccardi, G., Mastroddi, F.: semi-analytical unsteady aerodynamic modeling for a flexible thin airfoil in arbitrary motion. In: International Forum on Aeroelasticity and Structural Dynamic (2017)
32. Miao, J.-M., Ho, M.-H.: Effect of flexure on aerodynamic propulsive efficiency of flapping flexible airfoil. J. Fluids Struct. **22**, 401–419 (2006). https://doi.org/10.1016/j.jfluidstructs.2005.11.004
33. Zhou, C., Zhang, Y., Wu, J.: Effect of flexibility on unsteady aerodynamics forces of a purely plunging airfoil. Chin. J. Aeronaut. **33**, 88–101 (2020). https://doi.org/10.1016/j.cja.2019.08.002
34. Cook, J.R., Smith, M.J.: Stability of aeroelastic airfoils with camber flexibility. J. Aircr. **51**, 2024–2027 (2014). https://doi.org/10.2514/1.C032955
35. Anderson, J.D.: Fundamentals of aerodynamics. McGraw Hill Education, New York (2017)

36. Bisplinghoff, R.L., Halfman, R.: Aeroelasticity. Addison-Wesley Pub. Co., Cambridge (1955)
37. Gülçat, Ü.: Fundamentals of Modern Unsteady Aerodynamics. Springer Singapore, Singapore (2016)
38. Rao, S.S.: Vibration of Continuous Systems. Wiley, Hoboken (2019)

Publisher's Note Springer Nature remains neutral with regard to jurisdictional claims in published maps and institutional affiliations.